The critical role of cloud–infrared radiation feedback in tropical cyclone development

James H. Ruppert Jr[a,b,1], Allison A. Wing[c], Xiaodong Tang[d], and Erika L. Duran[e]

[a]Department of Meteorology and Atmospheric Science, The Pennsylvania State University, University Park, PA 16802; [b]Center for Advanced Data Assimilation and Predictability Techniques, The Pennsylvania State University, University Park, PA 16802; [c]Department of Earth, Ocean and Atmospheric Science, Florida State University, Tallahassee, FL 32306; [d]Key Laboratory of Mesoscale Severe Weather, Ministry of Education, and School of Atmospheric Sciences, Nanjing University, Nanjing 210093, China; and [e]Earth System Science Center, University of Alabama in Huntsville/NASA Short-term Prediction Research and Transition (SPoRT) Center, Huntsville, AL 35805

Edited by Kerry A. Emanuel, Massachusetts Institute of Technology, Cambridge, MA, and approved September 21, 2020 (received for review June 29, 2020)

The tall clouds that comprise tropical storms, hurricanes, and typhoons—or more generally, tropical cyclones (TCs)—are highly effective at trapping the infrared radiation welling up from the surface. This cloud–infrared radiation feedback, referred to as the "cloud greenhouse effect," locally warms the lower–middle troposphere relative to a TC's surroundings through all stages of its life cycle. Here, we show that this effect is essential to promoting and accelerating TC development in the context of two archetypal storms—Super Typhoon Haiyan (2013) and Hurricane Maria (2017). Namely, this feedback strengthens the thermally direct transverse circulation of the developing storm, in turn both promoting saturation within its core and accelerating the spin-up of its surface tangential circulation through angular momentum convergence. This feedback therefore shortens the storm's gestation period prior to its rapid intensification into a strong hurricane or typhoon. Further research into this subject holds the potential for key progress in TC prediction, which remains a critical societal challenge.

hurricane | radiation | tropical cyclone | clouds | feedback

Landfalling tropical cyclones (TCs) are among the most catastrophic natural disasters to affect humankind, which alone explain half of all weather- and climate-related deaths and economic losses in the United States (1). Upward trends in both population density and wealth in global coastal areas will continue exacerbating this issue (2), as will the rising sea level (3) and the likely increase of TC intensity with climate change (4–6). Major progress has been achieved in the prediction of TC motion in recent decades, owing to the increasing quantity and quality of satellite measurements and advancements in data assimilation (7–9). There has been comparatively little progress in the prediction of TC intensity and intensification, however, which underscores the need for further research into the physical processes that govern TC development (7).

The primary energy source for TCs is evaporation from the ocean surface (10). A long history of research indicates that TCs intensify through the WISHE feedback (wind-induced surface heat exchange), whereby the rate of evaporation increases with surface wind speed (11–13). A sufficiently strong initial surface cyclone is required for this process to ensue, however, and the pathway to this stage of TC genesis remains a subject of debate (14–17). This pathway is the focus of this study and is where we argue that cloud–radiation interaction plays a crucial role.

Two important discoveries suggest that TC development in nature may be acutely sensitive to cloud–radiation interaction. First, recent research highlights a pronounced diurnal variation in TCs—in their precipitation, clouds, and winds (18–25). This diurnal cycle is caused by the interaction between solar radiation and clouds in the TC (26–28), and thus implies that cloud–radiation interaction can substantially influence TC behavior. The second pertinent discovery is that the localized greenhouse effect of deep convective clouds has an important influence on TC development in idealized model frameworks (29–34). Namely, due to their extremely high emissivity, the deep convective clouds within an incipient storm locally increase the atmospheric trapping of infrared radiation, in turn locally warming the lower–middle troposphere relative to the storm's surroundings (35–39). This mechanism is a positive feedback to the incipient storm, as it promotes its thermally direct transverse circulation (38, 39) (Fig. 1*A*). Herein, we examine the role of this feedback in the context of TC development in nature.

In contrast to idealized study frameworks, TCs in nature develop from transient precursor disturbances, such as African easterly waves and monsoon depressions (40). Given such a disturbance, the variable large-scale environment conspires to promote its intensification into a strong TC only when sea surface temperature (SST) is high and vertical wind shear is suppressed (40), with few exceptions. Such constraints explain why TC development is fickle in nature. Assuming such conditions, the air within the precursor storm warms and moistens, as the convergence of angular momentum at low levels leads to the formation of a surface cyclone that can subsequently intensify through WISHE (14–17). Here, we test the hypothesis that cloud–infrared radiation feedback promotes and accelerates this evolution in the context of two archetypal storm events: Super Typhoon Haiyan (2013) (or Yolanda) and Hurricane Maria (2017). We conduct numerical modeling experiments using a small ensemble of large-scale, convection-resolving simulations and sensitivity tests for both storms using the Weather Research and Forecasting (WRF) atmosphere model (*Materials and Methods*). Given our objective,

Significance

The deep clouds that make up tropical disturbances, the precursors to more intense tropical cyclones (TCs) (including hurricanes and typhoons), effectively trap infrared radiation emitted by Earth's surface and lower atmosphere. Our results demonstrate that the local atmospheric warming caused by this "cloud greenhouse effect" is a key trigger for promoting and accelerating the evolution of such precursor storms into intense TCs. The forecasting of TC formation remains extremely challenging, while the representation of cloud processes and their feedback with radiation is a large source of uncertainty in the numerical models that forecasts rely upon. Our results suggest that focusing future research on constraining these processes in models holds promise for key progress in the prediction of these devastating storms.

Author contributions: J.H.R. designed research; J.H.R., A.A.W., X.T., and E.L.D. performed research; J.H.R. analyzed data; and J.H.R. wrote the paper.

The authors declare no competing interest.

This article is a PNAS Direct Submission.

[1]To whom correspondence may be addressed. Email: james.ruppert@psu.edu.

This article contains supporting information online at https://www.pnas.org/lookup/suppl/doi:10.1073/pnas.2013584117/-/DCSupplemental.

First published October 26, 2020.

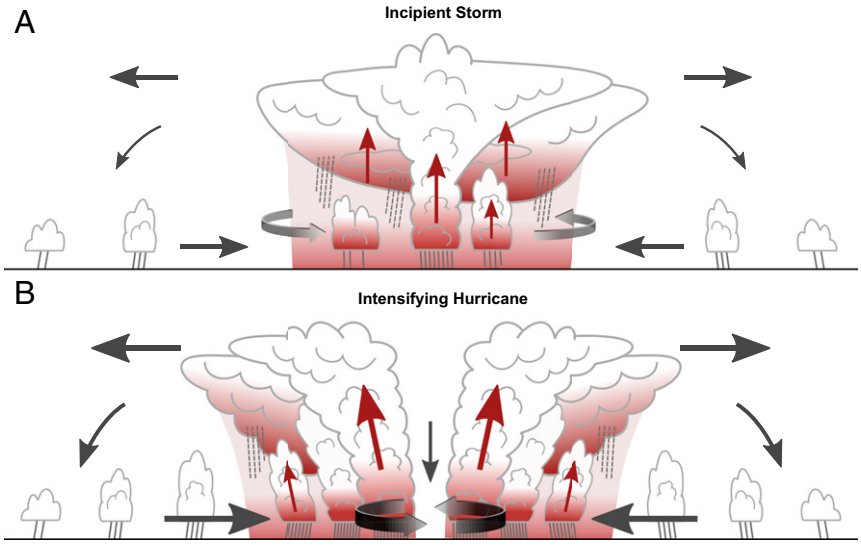

Fig. 1. The cloud greenhouse effect accelerates tropical cyclone development. Schematic depiction of how the trapping of infrared radiation by deep convective clouds leads to locally increased warming (red shading), and how this warming promotes the thermally direct transverse circulation (thin arrows) of the tropical cyclone (TC). (*A*) An incipient storm, characterized by a weak, broad primary circulation (thick, circular arrows). (*B*) An intensifying hurricane characterized by a well-defined eye and a strong primary circulation.

we focus herein on the initial formation and intensification of these events, neglecting their later evolution. An overview of the real and simulated storm events is provided next, followed by testing of the study hypothesis.

Overview of the Storm Events. Hurricane Maria and Super Typhoon Haiyan were both catastrophic, record-breaking storms due to their tracks and ideal environmental conditions for intensification prior to landfall—in the Lesser Antilles and Puerto Rico in the case of Maria, and in the Philippines in the case of Haiyan. However, both Haiyan and Maria developed along the typical pathways of storms in the Western North Pacific and Atlantic basins. They are therefore considered archetypal TC development cases, representative of a much larger sample of events. Below, we summarize the development of these storms by drawing from the official summaries of refs. (41) and (42).

Hurricane Maria was a classic Cape Verde hurricane, having developed from a disturbance that exited the west coast of Africa on 12 September 2017 and tracked west-northwestward under the influence of high pressure to its north (*SI Appendix*, Fig. S1*A*). Given favorable conditions of warm SST and weak vertical wind shear, the disturbance evolved rapidly: It reached hurricane status only 36 h after classification as a tropical depression and then underwent a period of extremely rapid intensification (RI) (defined as intensification by $\geq$16 m·s^{-1}·d^{-1}; 1 kt = 0.51 m·s^{-1}; Fig. 2*A* and *SI Appendix*, Fig. S2*C*). Maria then made landfall at 0115 UTC 19 September in Dominica as a category 5, with winds of 75 m·s^{-1} and the signature satellite-cloud appearance of an intense TC, including a cloud-free eye (Fig. 3*A*). Maria subsequently made another landfall in Puerto Rico as a category 4 hurricane (1015 UTC 20 September), although we focus herein on the period up to the first landfall, since this period captures its primary development phase.

Super Typhoon Haiyan originated as a disturbance within the monsoon trough near 7°N 162°E on 02 November 2013. Over the subsequent 24 h, it tracked westward to the south of Chuuk Atoll and began intensifying (Fig. 2*B* and *SI Appendix*, Fig. S1*B*). It was elevated to a tropical storm at 0000 UTC 04 November, and a typhoon by 0000 UTC 05 November. As with Maria, both high ocean heat content and weak vertical wind shear prompted a period of extreme RI (Fig. 2*B* and *SI Appendix*, Fig. S2*D*). Haiyan reached a maximum intensity of 87 m·s^{-1} by 1200 UTC 07 November, just before making landfall in the Philippines near Guiuan, Eastern Samar, around 0000 UTC 08 November (Fig. 3*B* and *SI Appendix*, Fig. S1*B*).

For both Maria and Haiyan, control simulations are conducted with the intent to reproduce their genesis and intensification realistically. The simulations are initialized 48 h prior to official storm identification in the case of Maria, and ~36 h prior in the case of Haiyan (start times of the observed time series are indicated by vertical ticks in Fig. 2 *A* and *B*). The intensity of the simulated storms is quantified by invoking two separate methods to calculate maximum wind speed. Fig. 2 *A* and *B* depicts the maximum azimuthally averaged 10 m wind speed, which effectively captures the intensity of the complete, closed circulation of the TC. This metric demonstrates that the control simulations for both Maria and Haiyan successfully capture TC genesis, beginning from negligible winds and ending with intense TCs. This metric, however, averages over more localized wind speed maxima, while such extrema are retained in the observed time series. Hence, for a fairer comparison with the observed time series, the wind speed maximum in the TC's vicinity without azimuthal averaging is depicted in *SI Appendix*, Fig. S2 *A* and *B* (the temporal maxima from this method are also depicted as abscissa crosses in Fig. 2 *A* and *B*). Both intensity metrics for the simulated storms demonstrate dramatic intensification, with periods of RI that endure for at least 24 h and maximum winds that reach 63 m·s^{-1} (category 4) in simulated Maria and 71 m·s^{-1} (category 5) in Haiyan (Fig. 2 *A* and *B* and *SI Appendix*, Fig. S2 *A–D*).

The time series also demonstrate that the simulated storms begin developing ~1 d later than in reality. This delay may owe to the initialization of these simulations using relatively coarse analysis datasets, without the incorporation of direct data assimilation procedures (*Materials and Methods*). The maximum wind speeds attained are also weaker than observed. This difference may owe in part to the delayed TC development prior to landfall, while it is also possible that higher wind speeds would be attained using a finer (e.g., 1-km) model grid.

The tracks of both simulated storms closely follow those of the real events, although with a slight northward bias, especially in Haiyan's case (*SI Appendix*, Fig. S1 *A* and *B*). Upon making

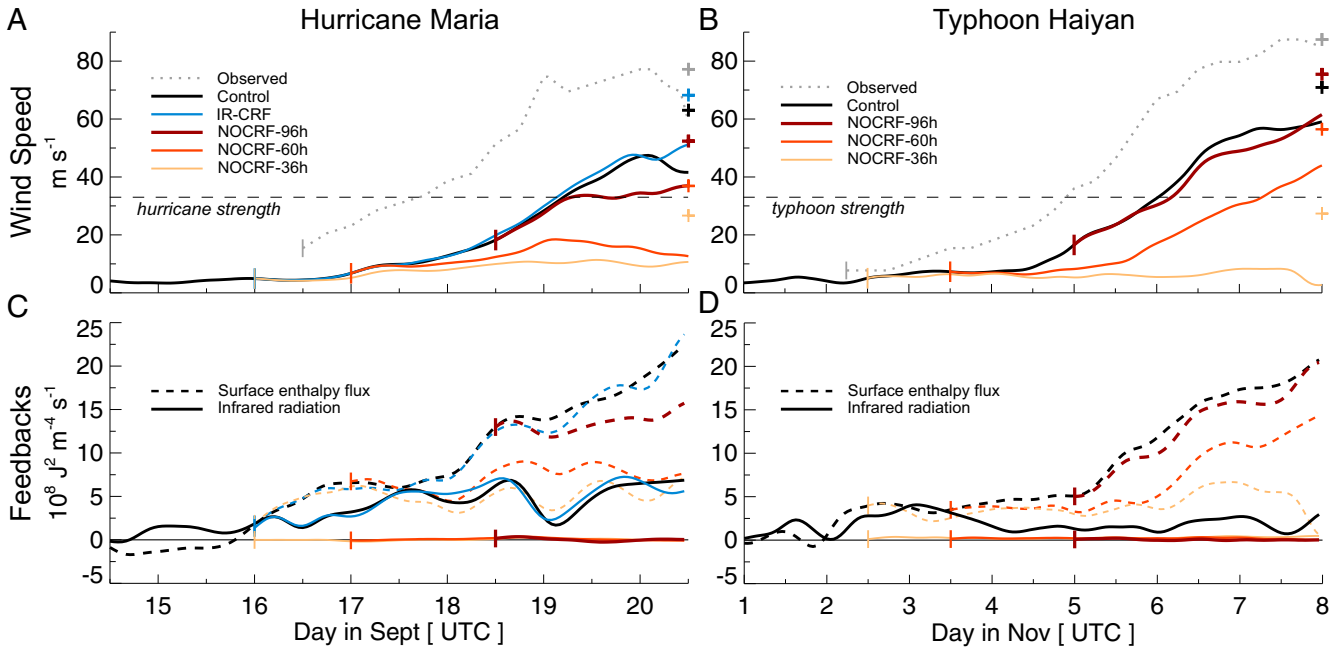

Fig. 2. Intensification and its energetic drivers. Time series of azimuthally averaged maximum wind speed at 10 m (*A* and *B*) and frozen moist static energy (MSE) feedback terms due to external (diabatic) sources (*C* and *D*): surface enthalpy flux (dashed) and infrared radiation (solid). Cloud–radiation interaction is turned off at the times indicated by the vertical ticks (in IR-CRF, cloud–infrared radiation interaction is retained). Maria tests at *Left* (*A* and *C*) and Haiyan tests at *Right* (*B* and *D*). Abscissa crosses denote maximum wind speed values without azimuthal averaging (cf. *SI Appendix*, Fig. S2 *A* and *B*).

landfall, the simulated storms have the appearance of strong TCs, with structures that are generally consistent with the observed storms (Fig. 3). Differences in their appearance likely owe, at least in part, to the simulated storms being slightly smaller in scale and weaker than the observed storms. Nonetheless, since the simulations adequately capture the genesis and intensification of these TC events to first order and closely follow the observed tracks, they are deemed sufficient to carry out the study objectives.

Role of Cloud–Infrared Radiation Feedback in Accelerating TC Development. We next test the hypothesis that cloud–infrared radiation feedback promotes and accelerates TC development by conducting a small ensemble of sensitivity tests: We initialize a set of simulations denoted "NOCRF-*h" (for no cloud–radiation forcing) as model restarts from the control simulations at select times (the asterisk denotes the restart time in hours since the start of the control). These tests are identical to the control simulations, although with all clouds made transparent to both

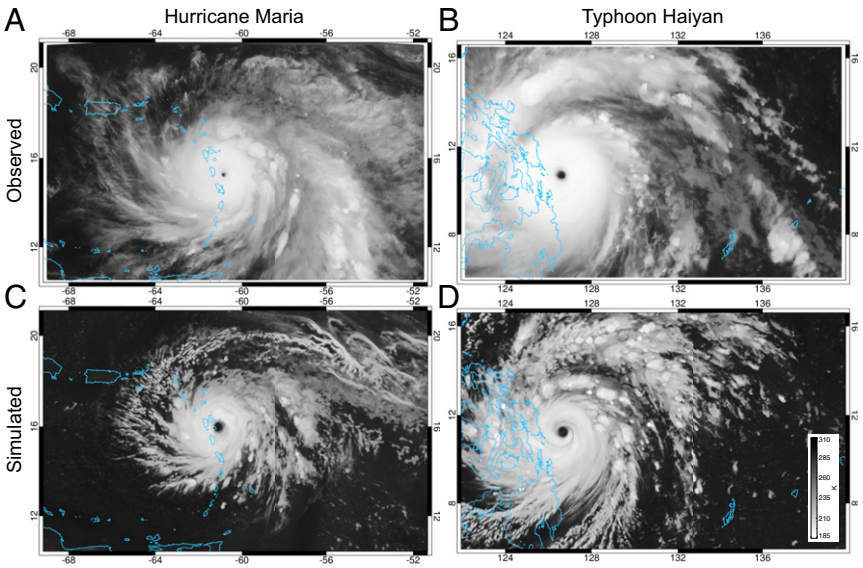

Fig. 3. Hurricane Maria and Typhoon Haiyan at peak intensity. Observed (*A* and *B*) and simulated (*C* and *D*) infrared brightness temperature (T_B; in kelvin) as measured by geostationary satellite for Maria (*A* and *C*) and Haiyan (*B* and *D*). (*A*) From *GOES-16* at 2245 UTC 18 September 2017; (*B*) from *MTSAT-1R* at 1830 UTC 07 November 2013; (*C*) from control simulation for Maria at 0400 UTC 20 September 2017; and (*D*) from control simulation for Haiyan at 0000 UTC 08 November 2013. Bright shading (cold temperatures) denotes clouds, especially deep and high clouds.

incoming solar and outgoing infrared radiation. Overall, this experiment for Maria demonstrates that cloud–radiation interaction has a profound, time-dependent impact on TC development (Fig. 2*A*). In NOCRF-36h, cloud–radiation interaction is removed roughly 48 h prior to RI (in the control), and as a result, intensification never ensues (*SI Appendix*, Fig. S2*C*). While intensification could hypothetically occur at a later time in this test (i.e., in a longer simulation), lengthening this gestation period by so long ($\gtrsim 2$ d) increases the probability that the incipient storm would either move over land or out of environmental conditions supportive for TC development, in turn lowering its probability of development. Furthermore, the test NOCRF-96h indicates that removing cloud–radiation interaction even after the onset of RI stifles the duration of intensification compared to the control. NOCRF-60h intensifies with some delay, and with maximum winds just barely exceeding hurricane strength (33 $m{\cdot}s^{-1}$; *SI Appendix*, Fig. S2*A*).

The experiment for Haiyan indicates qualitatively consistent results with those of Maria (Fig. 2*B*). Namely, NOCRF-36h exhibits no intensification through the end of the simulation, while intensification in NOCRF-60h is delayed by ∼1 d relative to the control. Different from the Maria experiment, however, the NOCRF-96h test of Haiyan exhibits intensification with very similar rate and timing to that in the control. This issue will be revisited later.

To isolate the specific role of cloud–infrared radiation interaction, we conduct an additional test for Maria denoted IR-CRF (i.e., infrared cloud–radiation forcing), which is identical to NOCRF-36h but with cloud–infrared radiation interaction retained within a radius of 800 km of the incipient TC (*Materials and Methods*). The similarity between TC development in the control and that in IR-CRF confirms that the infrared component of CRF is the critical aspect of cloud–radiation interaction for TC development (Fig. 2*A* and *SI Appendix*, Fig. S2*A*). This test therefore directly supports the hypothesis that cloud–infrared radiation feedback promotes and accelerates TC development in nature. This test also implies that cloud–solar radiation interaction (excluded from this test) plays a minimal role in promoting TC development (31), even though it is essential to the diurnal cycle in TCs (26–28).

Horizontal plan views of cloud at the final time step and wind speed history for the control and NOCRF-60h tests provide an informative view of the experiments (Fig. 4). The TC in the control for Maria exhibits a well-defined eye, and is associated with a swath of winds exceeding 50 $m{\cdot}s^{-1}$ (the threshold for category 3) (Figs. 3*C* and 4 *A* and *C*). In NOCRF-60h, however, the storm is poorly organized by the final simulation time, and in few locations do winds even reach hurricane strength (Fig. 4 *D* and *F*). Similar can be said of the Haiyan comparison: Although the TC in the NOCRF-60h test of Haiyan develops an eye, its cloud field is considerably smaller and winds much weaker than those of the control (Fig. 4 *G*, *I*, *J*, and *L*). The depictions of Haiyan's control test also portray the extremely large scale of its cloud and wind fields (Figs. 3*D* and 4 *G* and *I*). *SI Appendix*, Figs. S3 and S4 provide the corresponding depictions for all tests of the Maria and Haiyan experiments. We additionally conducted tests NOCRF-48h, NOCRF-72h, and NOCRF-84h for Maria, although since the results of these tests are highly consistent with the above findings, we do not discuss them.

To quantify the role of cloud–radiation feedback in TC development and place it into context with WISHE, we invoke frozen moist static energy (MSE)—the sum of latent and sensible heat and potential energy. MSE is conserved for phase change and changes in elevation, and hence provides an effective measure for the warming and moistening corresponding with TC development, as required by thermal wind balance (15–17, 33). We invoke the spatial variance budget of vertically integrated MSE to quantify the external, or diabatic, energy sources that promote TC development, following the approach of ref. 39 (*Materials and Methods*). These sources include infrared and solar radiative heating and surface turbulent enthalpy flux, the latter of which is dominated by wind speed effects on evaporation (31), and hence is a proxy for WISHE. Positive spatial covariance between MSE and these diabatic sources indicates a positive feedback promoting amplification of the incipient storm (31–33), and we quantify the feedbacks as such (Fig. 2 *C* and *D*). In the control simulations, WISHE dramatically increases with maximum wind speed, i.e., beginning on 18 September for Maria and 5 November for Haiyan, emphasizing its importance in TC intensification (Fig. 2 *A–D* and *SI Appendix*, Fig. S2 *A* and *B*). The feedback due to infrared radiation is also large in the control simulations, however, and is essentially equal in magnitude to WISHE during the period leading up to this intensification. The solar radiation feedback is on average much smaller than the infrared feedback (*SI Appendix*, Fig. S5). These relative magnitudes are consistent with results from idealized modeling studies (31–33).

The infrared feedback is negligible in all of the NOCRF-*h tests. In the NOCRF-36h and NOCRF-60h tests for Maria, wind speed never ramps up as it does in the control and IR-CRF, and hence WISHE remains comparatively stifled (Fig. 2*C*). These results emphasize the critical role of cloud–infrared radiation feedback in promoting the surface cyclone's genesis, and hence to the onset of RI via WISHE. Furthermore, the suppressed intensification in NOCRF-96h in the Maria experiment is associated with a suppressed increase of WISHE. This finding indicates that cloud–infrared radiation feedback remains important even during the RI stage of Maria, which acts by augmenting the WISHE feedback (24). As noted earlier, the NOCRF-96h test for Haiyan exhibits little difference from the control (Fig. 2*B* and *SI Appendix*, Fig. S2 *B* and *D*). The much lower magnitude of the infrared radiation feedback around the time this test is initialized from the control implies that this feedback plays a lesser role at this stage of intensification in the Haiyan experiment, in contrast to the Maria experiment (Fig. 2 *B* and *D*).

To visualize how the cloud greenhouse effect manifests in a positive MSE feedback, we confer with horizontal maps of IR'—vertically integrated infrared heating with the horizontal mean subtracted. In the control for Maria, IR' exhibits pronounced horizontal variance due to the contrast between areas with prevalent and suppressed deep convective cloud (Fig. 4 *A* and *B*). Since deep convection generally prevails where MSE is elevated, IR' covaries with MSE, constituting a positive feedback in the MSE spatial variance framework (Fig. 2*C*). With cloud–radiation feedback, and hence the cloud greenhouse effect, removed in NOCRF-60h, spatial variance in IR' is comparatively negligible, and hence its role as a source of MSE variance is greatly diminished (Fig. 4*E*). The IR' pattern for the control of Haiyan is similar in magnitude to that for Maria, with positive values closely corresponding to areas of cloud (Fig. 4 *G* and *H*). In NOCRF-60h, the magnitude of the IR' field is again greatly diminished (Fig. 4*K*).

Cloud–Infrared Radiation Feedback and the Transverse Circulation. The above analysis of the MSE variance budget excludes the impact of advection. While the budget term due to advection is likely substantial, it must be estimated, and with likely considerable error (31–33). Here, we instead assess how cloud–infrared radiation feedback directly affects the transverse circulation. The direct link between this feedback and the transverse circulation is important since the transverse circulation is responsible both for developing the TC's tangential circulation at low levels through angular momentum convergence and for importing moisture into its core. Moistening of the TC core is an essential feature of TC development, as intensification via WISHE feedback can only ensue with complete saturation in the core (14, 16, 43). The

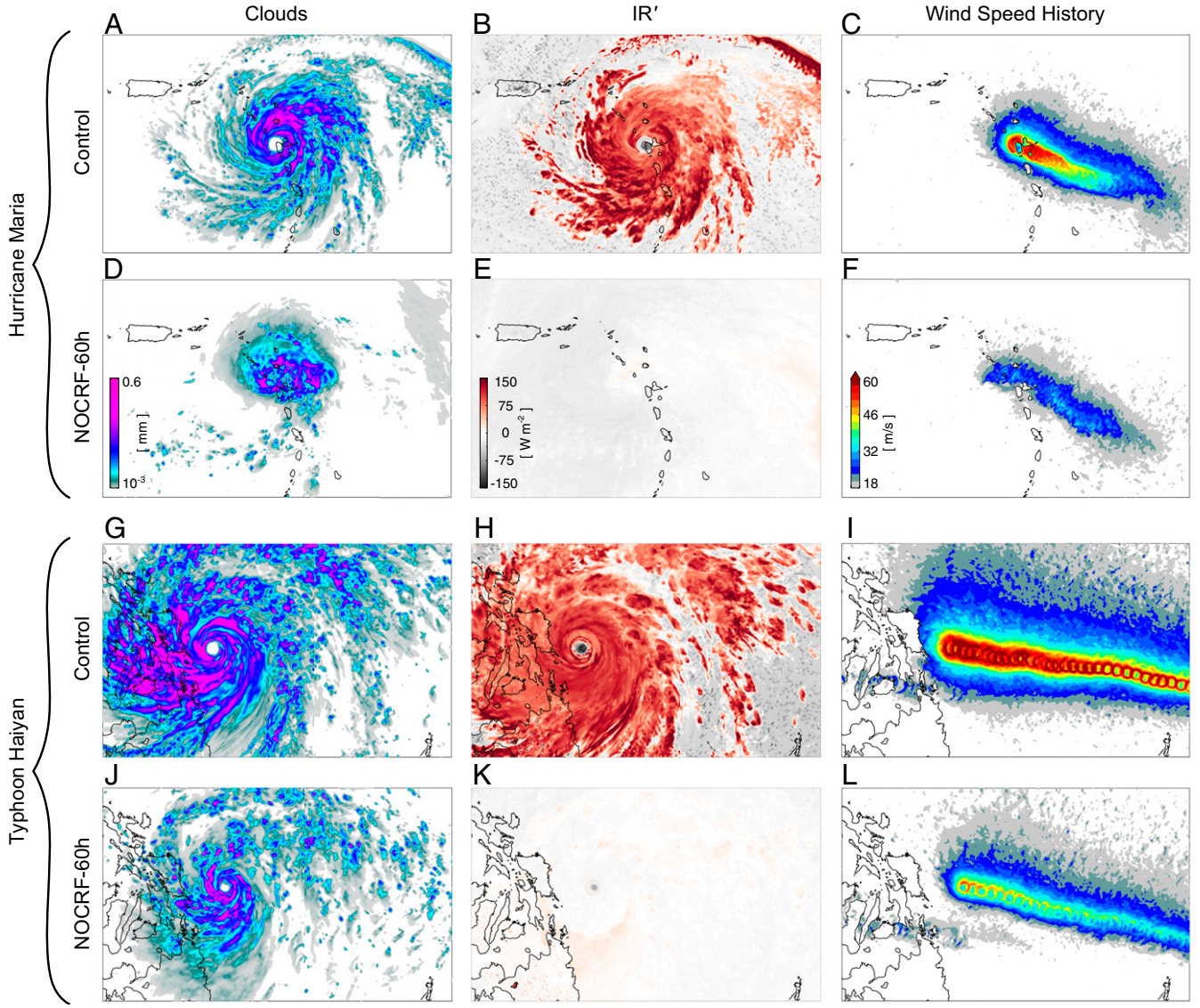

Fig. 4. Weaker storms with transparent clouds. (*A*) Vertically integrated cloud ice, (*B*) vertically integrated infrared radiative heating (IR) with the horizontal mean subtracted (IR′), and (*C*) maximum wind speed at 10 m from start to finish of the control simulation of Maria. (*D–F*) As in *A–C*, but for NOCRF-60 h of Maria, (*G–I*) the control simulation of Haiyan, and (*J–L*) NOCRF-60h of Haiyan. Cloud (*A*, *D*, *G*, and *J*) and IR′ (*B*, *E*, *H*, and *K*) are depicted at the final simulation time step. The apparent gaps in intense winds in *I* and *L* are an artifact of the TC's rapid westward motion between hourly model output time steps.

forthcoming analysis primarily emphasizes Maria for brevity, although we later extend the arguments to Haiyan to demonstrate their robustness.

The radial pattern of cloud–infrared radiation feedback within the incipient storm is crucial to its effect on TC development. A heat source localized in radius induces a thermally direct transverse circulation response, with ascending flow in the region of heating. When this heating is focused at radii less than the radius of maximum tangential winds (RMW) in the incipient storm, the low-level inward-flow component of this response efficiently converges angular momentum toward storm center, thereby promoting its intensification (44, 45). A vertical cross-section of IR′ averaged azimuthally around the incipient TC confirms that IR′ peaks inside of the RMW in the lower–middle troposphere in Maria in its early stage of development (Fig. 5*A*). Superimposed onto this cross section of IR′ is w_{crf}, the vertical component of the transverse circulation directly induced by IR′, which is diagnosed through the Sawyer–Eliassen equation with IR′ as the driving heat source (*Materials and Methods*). As expected, w_{crf} is greatest where IR′ maximizes, hence with a very bottom-heavy pattern of ascent. Horizontal convergence peaks where w_{crf} increases with height, i.e., from 0 to 2 km. This finding therefore indicates that cloud–infrared radiation feedback directly promotes the development of the surface cyclone by increasing angular momentum convergence.

We assess the role of w_{crf} in moistening the storm core by quantifying its influence on saturation in the incipient storm. Specifically, we assess the time scale in which upward moisture transport via w_{crf} will saturate the air through τ_{sat}, the ratio of saturation deficit to vertical moisture advection by w_{crf}:

$$\tau_{sat} \equiv \frac{q^* - q}{w_{crf}\partial q/\partial z},$$

where q is water vapor mixing ratio, q^* is that at saturation, z is height, and only regions where $w_{crf} > 0$ are considered. q and q^* are taken from the control simulation of Maria. Relative humidity

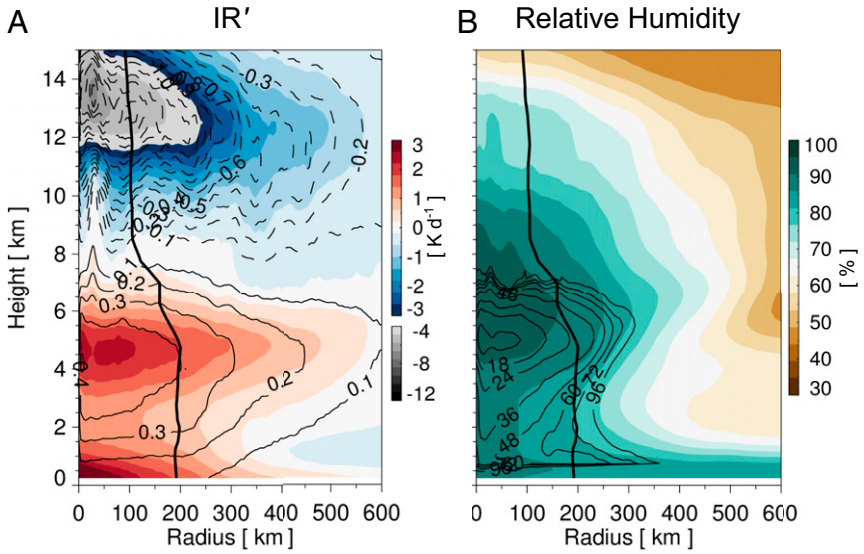

Fig. 5. The cloud greenhouse effect increases upward motion and moistening in the storm core. Azimuthally averaged vertical cross-sections of the incipient storm, averaged from 0000 UTC 16 to 0000 UTC 18 September in the control simulation for Maria. (*A*) IR′ (shading) and w_{crf}, the vertical component of the balanced circulation response to IR′ (contoured; cm·s^{-1}). (*B*) Relative humidity (shading) and τ_{sat}, the timescale in which lifting via w_{crf} will saturate the air (contoured; hours). The thick solid line denotes the radius of maximum tangential wind (RMW).

is depicted in Fig. 5*B* with τ_{sat} overlaid. τ_{sat} is lowest where air is closest to saturation and w_{crf} is greatest. Values of τ_{sat} are less than 24 h in a broad region from ∼4 to 6 km inside the RMW, indicating that radiatively induced lifting motion alone will saturate the middle troposphere in less than a day. While various external environmental factors may work against this effect and promote drying, these findings confirm that cloud–infrared radiation feedback directly promotes TC development by both increasing the low-level convergence of angular momentum and promoting saturation in the core of the developing cyclone.

The moistening due to this radiatively driven circulation permits a qualitative link back to the MSE variance budget. Namely, the moistening caused by the bottom-heavy structure of w_{crf} may contribute to increasing MSE spatial variance via the advective term (Fig. 5*A*). This effect represents a second pathway through which radiative forcing may directly promote MSE variance, and hence TC development, in addition to the direct diabatic feedback depicted in Fig. 2 *C* and *D* (31–33).

To assess how these effects vary in time, we next provide a time–radius view of vertically integrated IR′ and tangential wind. This view of the control for Maria demonstrates that IR′ maximizes inside of or near the RMW throughout the period leading up to RI (up to ∼1200 UTC 18 September) (Fig. 6*A*). The same can be said of the control for Haiyan (*SI Appendix*, Fig. S6*B*). Comparison between the control and NOCRF-60h for Maria reinforces the essential role of the cloud greenhouse effect in increasing the magnitude of IR′ (Fig. 6 *A* and *B*). Comparing vertical mass flux between the control and NOCRF-60h confirms that the transverse circulation weakens within hours after removing cloud–radiation interaction, and remains much weaker, corroborating that the cloud greenhouse effect directly promotes the transverse circulation (Fig. 6 *C* and *D*).

While the relative role of WISHE increases with TC intensity, it appears that cloud–infrared radiation feedback can remain important during the RI phase, as suggested by the NOCRF-96h test for Maria (Fig. 2 *A* and *C*). As RI ensues, the maximum in IR′ shifts radially outward due to the evolving distribution of clouds and development of a cloud-free eye, although it remains close to the RMW (Fig. 6*A*). This likely explains why the infrared MSE feedback remains appreciable through this period (Fig. 2*C*). Similar cannot be said of the Haiyan experiment, however, wherein IR′ eventually becomes widespread across outer radii and the infrared MSE feedback therefore decreases in magnitude (from ∼4 November onward) (Fig. 2*D* and *SI Appendix*, Fig. S6 *A* and *B*). These differences imply a need for further exploration into the role of radiative feedback during the RI stage.

Summary and Conclusions

In this study, we have investigated the role of cloud–infrared radiation feedback in TC formation and intensification through a set of convection-resolving numerical model experiments of Super Typhoon Haiyan (2013) and Hurricane Maria (2017). The results of these experiments demonstrate that cloud–infrared radiation feedback plays an essential role in promoting and accelerating TC development, as depicted schematically in Fig. 1. Namely, the greenhouse effect of deep convective clouds locally provides additional heat (MSE) to the incipient storm, which directly promotes its thermally direct transverse circulation. Since this excess heating is focused inside the radius of maximum tangential winds of the developing TC, it promotes cyclone spin-up by increasing the convergence of angular momentum. This radiatively induced circulation also promotes moistening and saturation of the storm core, which in turn primes the TC for intensification via WISHE feedback (Fig. 1*B*).

The two TC events that serve as foci in this study—Super Typhoon Haiyan (2013) and Hurricane Maria (2017)—were record-breaking events. However, they are also representative of the most common TC development pathway. These results therefore imply that cloud–infrared radiation feedback plays an essential role in the development of a large fraction of TC events in nature by dramatically shortening the gestation period prior to intensification. This timescale is crucial, given that the necessary conditions for TC genesis and intensification are typically limited both geographically and in time (40). Both the WISHE feedback and cloud–infrared radiation feedback should therefore be regarded as essential to TC development for most (i.e., archetypal) TC events in nature. While TC development can be captured in model frameworks that exclude interactive radiative forcing, the timescale of this development (from a representative precursor disturbance) is unlikely to be

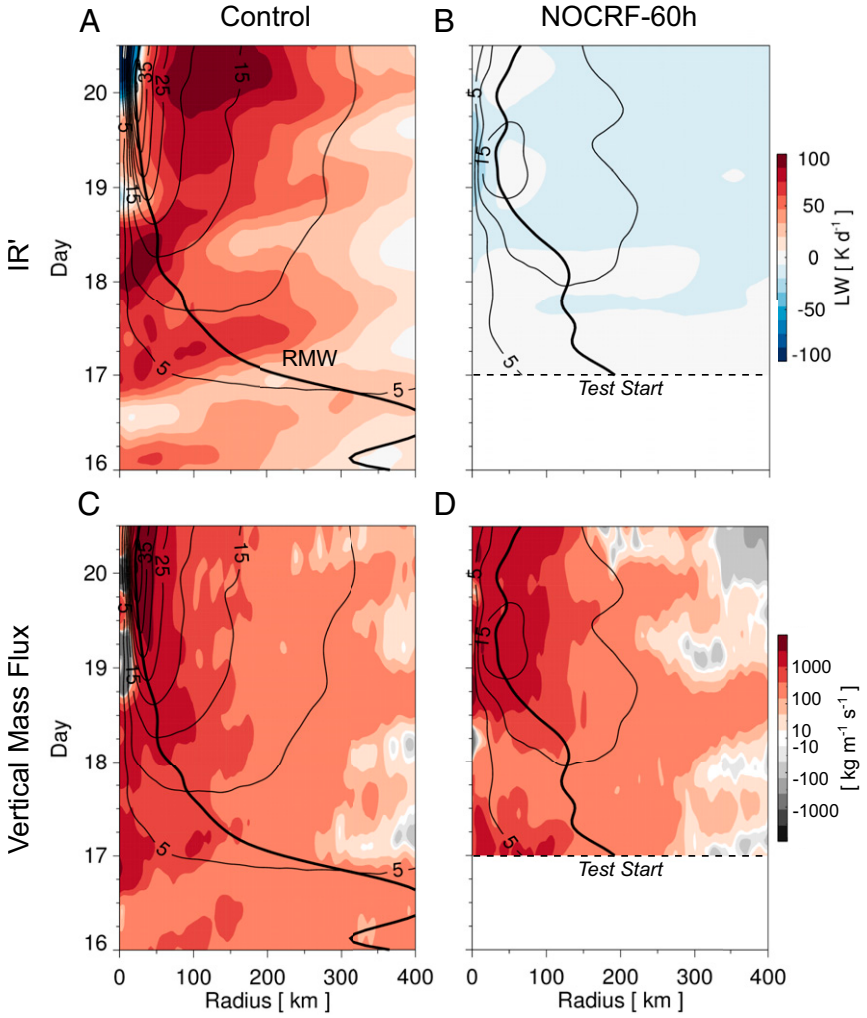

Fig. 6. TC development with and without the cloud greenhouse effect. Time–radius diagrams of vertically integrated IR′ (*A* and *B*) and vertical mass flux (*C* and *D*) in the control (*A* and *C*) and NOCRF-60h (*B* and *D*) simulations for Maria (time-axis labels are at 0000 UTC). Tangential wind at 10 m is contoured every 5 m·s^{-1}. The thick solid lines denote the RMW.

realistic in such frameworks. Confidence in these results is bolstered by the consensus among idealized studies of TC–radiation interaction (29–34). Further work is required, however, to assess whether these results apply to less common TC development pathways, such as TC intensification in the presence of strong vertical wind shear. Additionally, while we find evidence that this radiative feedback is also important during the rapid intensification stage in the case of Maria, this was not found in Haiyan, and hence this issue should be explored further.

The prediction of TC genesis and intensification remains a critical challenge (7). The results of this study imply that progress on this subject may be achieved through new efforts to better constrain the representation of cloud physics and radiative processes in the numerical models that TC forecasts strongly rely upon. New observational efforts to probe cloud and radiative processes in developing TCs would be highly valuable to this end. Studies of TC intensity prediction that can identify key sources of uncertainty in modern parameterizations of clouds and radiation would provide valuable guidance for such observational undertakings.

Several broader questions arise from this study. To what extent does the cloud–infrared radiation feedback affect the number of TCs that reach high intensity? Hypothetically, this feedback may promote the number of precursor disturbances that overcome environmental barriers to TC development, and hence reach high intensity. Furthermore, to what extent will TC behavior be affected by long-term changes in the vertical or horizontal distribution of clouds related to global climate change (46)? There is considerable uncertainty in projections of future TC activity, especially concerning their frequency (5, 6). A deeper understanding of how the mechanisms governing TC development may be changing will therefore be valuable for making progress on this issue.

Materials and Methods

TCs are categorized according to the Saffir–Simpson scale. Observed storm information for Maria comes from the HURDAT2 dataset provided by the National Oceanic and Atmospheric Administration (NOAA) National Hurricane Center (47), and that for Haiyan comes from the Joint Typhoon Warning Center (48).

Model Simulations of Typhoon Haiyan and Hurricane Maria. To investigate the development of Maria and Haiyan, a set of large-scale convection-resolving numerical model simulations is conducted using the Advanced Research Weather Research and Forecasting model (WRF-ARW; version 3.9.1.1) (49). A multistep simulation approach is taken to represent the various key scales of motion, wherein static (i.e., nonmoving) nests are invoked to simulate the TCs. First, a three-nested-domain simulation ("3Dom") is conducted for both storm events, with horizontal grid spacing of 27, 9, and 3 km from the

largest to smallest domain, with two-way domain feedback between the domains. These model domains are shown in *SI Appendix*, Fig. S7. The outermost (largest) domain for Haiyan extends from 72.1°E–177.9°E and 27.8°S–36.2°N, while that for Maria extends from 117.9°W–12.1°W and 8.1°S–51.2°N. The simulation for Haiyan is integrated from 0000 UTC 1 to 0000 UTC 8 November 2013, while that for Maria is integrated from 1200 UTC 14 to 1200 UTC 20 September 2017. Next, using hourly output from the middle domain of the 3Dom simulations, WRF-NDOWN is invoked to generate new lateral boundary conditions for the innermost domain. These new time-varying boundary conditions are then imposed for all simulations analyzed in the study, which are conducted only on the innermost (3-km) model domain. Since these boundary conditions are invariant between sensitivity tests for each storm, the potential spurious impacts of large-scale drift between tests are alleviated.

The control simulation for each storm invokes realistic physics settings and is conducted on the 3-km model domain as described above. Sensitivity simulations denoted "NOCRF-*h" are then conducted, which are restarts from the control at the time "*" (in hours) after the start time of the control. These tests are identical to the control except with cloud–radiation interaction removed by excluding all hydrometeors from both the infrared and solar radiation calculations. An additional test for Maria denoted "IR-CRF" is conducted, which is identical to NOCRF-36h but with cloud–infrared radiation interaction retained within a specified radius of TC center, as follows. During model runtime, we calculate the cloud–radiation forcing at a point as $Q_{cloud} = Q - Q_{clear}$, where Q is the radiative forcing including interaction with clouds and Q_{clear} is that excluding it (i.e., as in NOCRF-*h). We then impose the radiative forcing at each time step as $Q = Q_{clear} + \alpha\, Q_{cloud}$, where $\alpha = 1$ for radius $r < 600$ km, $\alpha = 800 - r/200$ for r: 600 to 800 km, and $\alpha = 0$ for radius $r > 800$ km.

Model initial and outer-boundary conditions come from six-hourly National Centers for Environmental Prediction Global Forecast System model analyses. For Hurricane Maria, analyses are retrieved at 0.25° grid spacing from the National Center for Atmospheric Research–University Corporation for Atmospheric Research Data Archive (50), and for Typhoon Haiyan, they are retrieved at 0.5° spacing from NOAA (51). The coarseness of these datasets relative to the 3-km innermost model domain likely accounts for the delayed TC development in the control simulations compared to the real events (Fig. 2 *A* and *B*). Namely, the development of convection down at the 3-km grid-scale requires approximately 1 d, which in turn likely stalls TC development. We do not probe this issue herein, however, as the TC development captured by the control simulations is deemed adequate to achieve the study objectives.

Radiation is treated using the rapid radiative transfer model infrared radiation scheme (52) and Dudhia solar scheme (53), which are called every 3 min in the innermost domain (9 and 27 min in the middle and outermost domains, respectively). Cloud processes are represented using the WRF single-moment six-class scheme (54). Additional parameterizations invoked include the YSU vertical diffusion scheme (55), the revised MM5 surface layer scheme (56), a skin SST scheme (57), and the Donelan et al. (58) scheme for calculating surface enthalpy and drag exchange coefficients. A cumulus parameterization (59) is invoked for the outermost model domain for 3Dom. The model time steps for 3Dom are 90, 30, and 10 s from largest to smallest domain, and 10 s for the single domain of the main simulations. All domains invoke a stretched vertical grid of 55 levels, with model top at 10 hPa. The complete model code and runtime specifications (including model namelists) employed are archived in a public repository (60).

Hourly model output is employed for all postprocessing. TC location is tracked in each simulation as the hourly local maximum of absolute vertical vorticity at 700 hPa, after horizontal filtering using 1.5° horizontal boxcar smoothing. Unless otherwise specified, all vertical integrals are computed using mass-weighting as $[] = 1/g \int_{p_{top}}^{p_0} [] dp$, where p is pressure, g is gravity, $p_0 = 1{,}000$ hPa, and $p_{top} = 100$ hPa.

Satellite Cloud Brightness Temperature. Depictions of cloud in Fig. 3 *A* and *B* are top-of-atmosphere radiant brightness temperature T_B in the infrared or longwave window measured by radiometers onboard geostationary satellites (*GOES-16* for Maria; *MTSAT-1R* for Haiyan). The spectral bands of these radiance measurements are centered at 11.2 μm for Maria (channel 14 of the Advanced Baseline Imager, or ABI, onboard *GOES-16*) and 10.8 μm for Haiyan (channel IR1 of the Japanese Advanced Meteorological Imager onboard *MTSAT-1R*). *GOES-16* data are retrieved from NOAA (61). *MTSAT-1R* data are retrieved from Meteorological Agency, Weathernews, Takeuchi Lab of the Earthquake Research Institute of the University of Tokyo, and Chiba University (62).

To produce the corresponding T_B measurements for WRF model simulations, the community radiative transfer model (CRTM) [version 2.3.0; (63)] is used to convert WRF model output to simulated T_B measurements corresponding to the same satellites and spectral channels. These simulated T_B measurements may have biases due to errors in the WRF model microphysics schemes and/or CRTM, but are nonetheless suitable for an overarching depiction of clouds in the simulated TCs. All code necessary to conduct this analysis is archived in a public repository (60).

MSE Feedbacks. The frozen MSE diabatic feedback terms depicted in Fig. 2 and *SI Appendix*, Fig. S5 are calculated as the sources of MSE spatial variance for a moving TC-centered box of 10° in latitude and longitude, as follows. MSE is first calculated as $h = c_p T + gz + L_v q_v - L_f q_{ice}$, where c_p is the specific heat of dry air at constant pressure, T is temperature, g is gravity, z is height, q_v is water vapor mixing ratio, q_{ice} is total frozen condensate mixing ratio, and $L_v = L_v(T)$ and $L_f = L_f(T)$ are the latent heats of vaporization and fusion, respectively. Next, h is vertically integrated using mass-weighting as $\hat{h} = 1/g \int_{p_{top}}^{p_0} h dp$, where $p_0 = 950$ hPa [to account for the lowering of pressure surfaces as the vortex intensifies (33)] and $p_{top} = 100$ hPa. The three diabatic sources of $\hat{h}$ are IR, solar radiative heating SO, and surface enthalpy flux (SEF) (the sum of turbulent sensible and latent heat flux). Both IR and SO are vertically integrated using mass-weighting from the surface to 100 hPa. As described in ref. 39, the diabatic feedback terms are then computed as $\hat{h}'IR'$, $\hat{h}'SO'$, and $\hat{h}'SEF'$, respectively, where the primes denote anomalies from the horizontal mean over the sampling box.

Balanced Circulation Response to Cloud Greenhouse Effect. The impact of the cloud greenhouse effect on the transverse circulation of the incipient TC is quantified as the balanced circulation response to IR′, using the axisymmetric Sawyer–Eliassen equation. This approach yields a conservative estimate of this impact, as it excludes nonlinearity related to the feedback between radiation, circulation, and SEF. The imposed heat forcing is computed by averaging azimuthal mean IR in time from 0000 UTC 16 to 0000 UTC 18 September in the control simulation for Maria, with the radius-normalized mean subtracted at each level. The result, IR′, is depicted in Fig. 5*A*. This forcing includes clear-air infrared cooling, although it is dominated by cloud effects (e.g., Fig. 4 *B* and *E*). The circulation equation and procedures for computing its solution follow ref. 64. We compute this solution from 0 to 1,000 km in radius. The thermodynamic base state is prescribed using state variables from the control simulation over the same time period and area. The prescribed idealized base-state vortex is based on the tangential wind field of the control simulation averaged over this time period; it is characterized by a maximum tangential wind speed of 8 $m \cdot s^{-1}$ and RMW of 200 km. All settings for this calculation, the imposed heat forcing, and the thermodynamic base-state sounding are archived in a public repository (60).

Temporal Filtering. Temporal filtering is applied to highlight key signals and alleviate noise. Time series in Fig. 2 and *SI Appendix*, Figs. S2 and S5 are filtered using a Gaussian kernel with a three-point (i.e., 3-h) SD, with the exception of intensification rate; for intensification rate (*SI Appendix*, Fig. S2 *C* and *D*), maximum wind speed at 10 m is first filtered using a Gaussian kernel with a six-point SD, and the time derivative is then taken using three-point Lagrangian interpolation. Variables in Fig. 6 and *SI Appendix*, Fig. S6 are temporally filtered using a Gaussian kernel with a three-point SD.

Data Availability. All model and postprocessing code necessary to replicate the results of this study have been archived in a public repository (60) or are cited in the *Materials and Methods*.

ACKNOWLEDGMENTS. Fuqing Zhang, Robert Nystrom, and Kerry Emanuel are acknowledged for helpful comments. Hugh Willoughby is acknowledged for providing solver code for Sawyer–Eliassen calculations. We also thank Yunji Zhang and Masashi Minamide for guidance on the use of infrared satellite data and CRTM code. We thank two anonymous reviewers for their helpful comments. J.H.R. received support from the Center for Advanced Data Assimilation and Predictability Techniques, the Pennsylvania State University; A.A.W. from NOAA's Climate Program Office's Modeling, Analysis, Predictions, and Projections Program under Grant NA18OAR4310270 and the NSF through Grant 1830724; X.T. from the National Key R&D Program of China under Grant 2017YFC1501601 and the National Natural Science Foundation of China through Grant 41675054; and E.L.D. from Tsengdar Lee of NASA's Research and Analysis Program, Weather Focus Area through the Short-term Prediction Research and Transition Center.

1. NOAA National Centers for Environmental Information (NCEI), Billion-dollar weather and climate disasters. https://www.doi.org/10.25921/stkw-7w73. Accessed 12 April 2020.
2. R. A. Pielke Jr., Future economic damage from tropical cyclones: Sensitivities to societal and climate changes. *Philos. Trans. A Math. Phys. Eng. Sci.* **365**, 2717–2729 (2007).
3. J. D. Woodruff, J. L. Irish, S. J. Camargo, Coastal flooding by tropical cyclones and sea-level rise. *Nature* **504**, 44–52 (2013).
4. K. Emanuel, Will global warming make hurricane forecasting more difficult? *Bull. Am. Meteorol. Soc.* **98**, 495–501 (2017).
5. T. Knutson *et al*., Tropical cyclones and climate change assessment: Part I: Detection and attribution. *Bull. Am. Meteorol. Soc.* **100**, 1987–2007 (2019).
6. T. Knutson *et al*., Tropical cyclones and climate change assessment: Part II: Projected response to anthropogenic warming. *Bull. Am. Meteorol. Soc.* **101**, E303–E322 (2020).
7. M. DeMaria, C. R. Sampson, J. A. Knaff, K. D. Musgrave, Is tropical cyclone intensity guidance improving? *Bull. Am. Meteorol. Soc.* **95**, 387–398 (2014).
8. P. Bauer, A. Thorpe, G. Brunet, The quiet revolution of numerical weather prediction. *Nature* **525**, 47–55 (2015).
9. R. B. Alley, K. A. Emanuel, F. Zhang, Advances in weather prediction. *Science* **363**, 342–344 (2019).
10. H. Riehl, A model of hurricane formation. *J. Appl. Phys.* **21**, 917–925 (1950).
11. E. Kleinschmidt, Grundlagen einer Theorie der Tropischen Zyklonen. *Arch. für Meteorol. Geophys. und Bioklimatologie Ser. A* **4**, 53–72 (1951).
12. K. A. Emanuel, An air-sea interaction theory for tropical cyclones. Part I: Steady-state maintenance. *J. Atmos. Sci.* **43**, 585–605 (1986).
13. F. Zhang, K. Emanuel, On the role of surface fluxes and WISHE in tropical cyclone intensification. *J. Atmos. Sci.* **73**, 2011–2019 (2016).
14. K. A. Emanuel, The finite-amplitude nature of tropical cyclogenesis. *J. Atmos. Sci.* **46**, 3431–3456 (1989).
15. M. T. Montgomery, M. E. Nicholls, T. A. Cram, A. B. Saunders, A vortical hot tower route to tropical cyclogenesis. *J. Atmos. Sci.* **63**, 355–386 (2006).
16. D. S. Nolan, What is the trigger for tropical cyclogenesis? *Aust. Meteorol. Mag.* **56**, 241–266 (2007).
17. S. Gjorgjievska, D. J. Raymond, Interaction between dynamics and thermodynamics during tropical cyclogenesis. *Atmos. Chem. Phys.* **14**, 3065–3082 (2014).
18. J. P. Kossin, Daily hurricane variability inferred from GOES infrared imagery. *Mon. Weather Rev.* **130**, 2260–2270 (2002).
19. J. P. Dunion, C. D. Thorncroft, C. S. Velden, The tropical cyclone diurnal cycle of mature hurricanes. *Mon. Weather Rev.* **142**, 3900–3919 (2014).
20. C. Melhauser, F. Zhang, Diurnal radiation cycle impact on the pregenesis environment of Hurricane Karl (2010). *J. Atmos. Sci.* **71**, 1241–1259 (2014).
21. K. P. Bowman, M. D. Fowler, The diurnal cycle of precipitation in tropical cyclones. *J. Clim.* **28**, 5325–5334 (2015).
22. X. Tang, F. Zhang, Impacts of the diurnal radiation cycle on the formation, intensity, and structure of Hurricane Edouard (2014). *J. Atmos. Sci.* **73**, 2871–2892 (2016).
23. J. A. Knaff, C. J. Slocum, K. D. Musgrave, Quantification and exploration of diurnal oscillations in tropical cyclones. *Mon. Weather Rev.* **147**, 2105–2121 (2019).
24. X. Tang, Z.-M. Tan, J. Fang, E. B. Munsell, F. Zhang, Impact of the diurnal radiation contrast on the contraction of radius of maximum wind during intensification of Hurricane Edouard (2014). *J. Atmos. Sci.* **76**, 421–432 (2019).
25. J. A. Zhang, J. P. Dunion, D. S. Nolan, In situ observations of the diurnal variation in the boundary layer of mature hurricanes. *Geophys. Res. Lett.* **47**, 2019GL086206 (2020).
26. E. L. Navarro, G. J. Hakim, H. E. Willoughby, Balanced response of an axisymmetric tropical cyclone to periodic diurnal heating. *J. Atmos. Sci.* **74**, 3325–3337 (2017).
27. J. H. Ruppert, M. E. O'Neill, Diurnal cloud and circulation changes in simulated tropical cyclones. *Geophys. Res. Lett.* **46**, 502–511 (2019).
28. R. C. Evans, D. S. Nolan, Balanced and radiating wave responses to diurnal heating in tropical cyclone-like vortices using a linear nonhydrostatic model. *J. Atmos. Sci.* **76**, 2575–2597 (2019).
29. Y. P. Bu, R. G. Fovell, K. L. Corbosiero, Influence of cloud–radiative forcing on tropical cyclone structure. *J. Atmos. Sci.* **71**, 1644–1662 (2014).
30. M. E. Nicholls, An investigation of how radiation may cause accelerated rates of tropical cyclogenesis and diurnal cycles of convective activity. *Atmos. Chem. Phys.* **15**, 9003–9029 (2015).
31. A. A. Wing, S. J. Camargo, A. H. Sobel, Role of radiative–convective feedbacks in spontaneous tropical cyclogenesis in idealized numerical simulations. *J. Atmos. Sci.* **73**, 2633–2642 (2016).
32. C. J. Muller, D. M. Romps, Acceleration of tropical cyclogenesis by self-aggregation feedbacks. *Proc. Natl. Acad. Sci. U.S.A.* **115**, 2930–2935 (2018).
33. A. A. Wing *et al*., Moist static energy budget analysis of tropical cyclone intensification in high-resolution climate models. *J. Clim.* **32**, 6071–6095 (2019).
34. W. P. Smith, M. E. Nicholls, R. A. Pielke, The role of radiation in accelerating tropical cyclogenesis in idealized simulations. *J. Atmos. Sci.* **77**, 1261–1277 (2020).
35. D. J. Raymond, X. Zeng, Instability and large-scale circulations in a two-column model of the tropical troposphere. *Q. J. R. Meteorol. Soc.* **126**, 3117–3135 (2000).
36. C. S. Bretherton, P. N. Blossey, M. Khairoutdinov, An energy-balance analysis of deep convective self-aggregation above uniform SST. *J. Atmos. Sci.* **62**, 4273–4292 (2005).
37. C. J. Muller, I. M. Held, Detailed investigation of the self-aggregation of convection in cloud-resolving simulations. *J. Atmos. Sci.* **69**, 2551–2565 (2012).
38. K. Emanuel, A. A. Wing, E. M. Vincent, Radiative-convective instability. *J. Adv. Model. Earth Syst.* **6**, 75–90 (2014).
39. A. A. Wing, K. A. Emanuel, Physical mechanisms controlling self-aggregation of convection in idealized numerical modeling simulations. *J. Adv. Model. Earth Syst.* **6**, 59–74 (2014).
40. W. M. Gray, Global view of the origin of tropical disturbances and storms. *Mon. Weather Rev.* **96**, 669–700 (1968).
41. R. J. Pasch, A. B. Penny, R. Berg, National Hurricane Center tropical cyclone report: Hurricane Maria (AL152017). https://www.nhc.noaa.gov/data/tcr/AL152017_Maria.pdf. Accessed 1 May 2019.
42. A. D. Evans, R. J. Falvey, Annual tropical cyclone report 2013. http://go.nature.com/V9JpKu. Accessed 5 July 2019.
43. M. Bister, K. A. Emanuel, The genesis of Hurricane Guillermo: TEXMEX analyses and a modeling study. *Mon. Weather Rev.* **125**, 2662–2682 (1997).
44. J. L. Vigh, W. H. Schubert, Rapid development of the tropical cyclone warm core. *J. Atmos. Sci.* **66**, 3335–3350 (2009).
45. K. D. Musgrave, R. K. Taft, J. L. Vigh, B. D. McNoldy, W. H. Schubert, Time evolution of the intensity and size of tropical cyclones. *J. Adv. Model. Earth Syst.* **4**, M08001 (2012).
46. T. W. Cronin, A. A. Wing, Clouds, circulation, and climate sensitivity in a radiative-convective equilibrium channel model. *J. Adv. Model. Earth Syst.* **9**, 2883–2905 (2017).
47. C. W. Landsea, J. L. Franklin, Atlantic hurricane database uncertainty and presentation of a new database format. *Mon. Weather Rev.* **141**, 3576–3592 (2013).
48. Joint Typhoon Warning Center, Western North Pacific Ocean Best Track Data. https://www.metoc.navy.mil/jtwc/jtwc.html?western-pacific. Accessed 5 July 2019.
49. W. C. Skamarock *et al*, "A description of the advanced research WRF, version 3" (Tech. Rep. NCAR/TN-475+STR, National Center for Atmospheric Research–University Corporation for Atmospheric Research, 2008).
50. National Centers for Environmental Prediction/National Weather Service/NOAA/US Department of Commerce, NCEP GFS 0.25 Degree Global Forecast Grids Historical Archive. National Center for Atmospheric Research, Computational and Information Systems Laboratory. https://doi.org/10.5065/D65D8PWK. Accessed 1 May 2019.
51. NOAA National Centers for Environmental Information, Global Forecast System (GFS). https://www.ncdc.noaa.gov/data-access/model-data/model-datasets/global-forcast-system-gfs. Accessed 5 July 2019.
52. E. J. Mlawer, S. J. Taubman, P. D. Brown, M. J. Iacono, S. A. Clough, Radiative transfer for inhomogeneous atmospheres: RRTM, a validated correlated-k model for the longwave. *J. Geophys. Res.* **102**, 16663 (1997).
53. J. Dudhia, Numerical study of convection observed during the winter monsoon experiment using a mesoscale two-dimensional model. *J. Atmos. Sci.* **46**, 3077–3107 (1989).
54. S.-Y. Hong, J.-O. J. Lim, The WRF single-moment 6-class microphysics scheme (WSM6). *J. Korean Meteorol. Soc.* **43**, 129–151 (2006).
55. S. Hong, Y. Noh, J. Dudhia, A new vertical diffusion package with an explicit treatment of entrainment processes. *Mon. Weather Rev.* **134**, 2318–2341 (2006).
56. P. A. Jiménez *et al*., A revised scheme for the WRF surface layer formulation. *Mon. Weather Rev.* **140**, 898–918 (2012).
57. X. Zeng, A. Beljaars, A prognostic scheme of sea surface skin temperature for modeling and data assimilation. *Geophys. Res. Lett.* **32**, L14605 (2005).
58. M. A. Donelan *et al*., On the limiting aerodynamic roughness of the ocean in very strong winds. *Geophys. Res. Lett.* **31**, L18306 (2004).
59. G. A. Grell, S. R. Freitas, A scale and aerosol aware stochastic convective parameterization for weather and air quality modeling. *Atmos. Chem. Phys.* **14**, 5233–5250 (2014).
60. J. H. Ruppert, A. A. Wing, X. Tang, E. L. Duran, Dataset for "The critical role of cloud–infrared radiation feedback in tropical cyclone development." Penn State Data Commons. https://doi.org/10.26208/9myk-nh50. Deposited 5 May 2020.
61. NOAA National Centers for Environmental Information, GOES-R Algorithm Working Group, GOES-R Series Program, NOAA GOES-R Series Advanced Baseline Imager (ABI) Level 2 Cloud and Moisture Imagery Products, channel 14. https://doi.org/10.7289/V5736P36. Accessed 20 August 2020.
62. Meteorological Agency, Weathernews, and Takeuchi Lab of the Earthquake Research Institute of the University of Tokyo, CEReS Center for Environmental Remote Sensing Chiba University Database, MTSAT-1R. http://www.cr.chiba-u.jp/japanese/database.html. Accessed 24 August 2020.
63. J. D. Han *et al*., JCSDA community radiative transfer model (CRTM)–Version 1. *NOAA Tech. Rep. NESDIS* **122**, 40 (2006).
64. A. G. Pendergrass, H. E. Willoughby, Diabatically induced secondary flows in tropical cyclones. Part I: Quasi-steady forcing. *Mon. Weather Rev.* **137**, 805–821 (2009).